JVST A
Journal of Vacuum Science & Technology A

ARTICLE

avs.scitation.org/journal/jva

Improved properties of atomic layer deposited ruthenium via postdeposition annealing

Cite as: J. Vac. Sci. Technol. A 39, 052402 (2021); doi: 10.1116/6.0001078
Submitted: 8 April 2021 · Accepted: 7 July 2021 ·
Published Online: 27 July 2021

Michael Hayes,[1] Melanie A. Jenkins,[1] Jacob Woodruff,[2] Daniel F. Moser,[3] Charles L. Dezelah,[2,a)] and John F. Conley, Jr.[1,b)]

AFFILIATIONS

[1]Department of Electrical Engineering, Oregon State University, 1148 Kelley Engineering Center, Corvallis, Oregon 97333
[2]EMD Performance Materials, Haverhill, Massachusetts, 01832
[3]EMD Performance Materials, 5485 County Road, Sheboygan Falls, Wisconsin 53085

Note: This paper is part of the 2022 Special Topic Collection on Atomic Layer Deposition (ALD).
[a)]**Present address:** ASM Microchemistry Oy, Pietari Kalmin katu 3 F 2, 00560 Helsinki, Finland.
[b)]**Author to whom correspondence should be addressed:** jconley@eecs.oregonstate.edu

ABSTRACT

The resistivity, morphology, and effective work function of thin film ruthenium deposited by thermal atomic layer deposition (ALD) using η^4-2,3-dimethylbutadiene ruthenium tricarbonyl [Ru(DMBD)$(CO)_3$] and O_2 are investigated before and after annealing at temperatures up to 500 °C. Annealing at 500 °C in either N_2 or H_2/N_2 reduces the average resistivity of as-deposited 30 nm thick Ru films from 16.2 to as low as 13.7 or 9.1 $\mu\Omega$ cm, respectively, approaching the bulk value of Ru. X-ray diffraction shows that as-deposited films are polycrystalline hexagonal Ru. Annealing at 500 °C in either N_2 or H_2/N_2 results in crystallite growth accompanied by a roughening of the surface from approximately 0.7 to 2.2 nm RMS, as shown by atomic force microscopy. Secondary ion mass spectroscopy shows low residual carbon and oxygen in as-deposited films. Annealing in N_2 at 500 °C reduces only the carbon content, whereas annealing in H_2/N_2 at 500 °C results in a further reduction of carbon combined with reduction in oxygen as well. Using series of metal/oxide/silicon capacitors with varying oxide thickness, the effective work function of 500 °C H_2/N_2 annealed Ru films on ALD Al_2O_3 and HfO_2 was determined to be approximately 4.9 and 5.3 eV, respectively. Using internal photoemission spectroscopy, the Ru/Al_2O_3 and Ru/HfO_2 electron energy barrier heights were determined to be 3.4 ± 0.1 and 3.8 ± 0.1 eV, respectively.

I. INTRODUCTION

Ruthenium metal is promising for several applications in the microelectronics industry, including its use as a conductive metal for integrated circuit (IC) interconnects and as a gate electrode for metal/oxide/semiconductor (MOS) and metal/insulator/metal (MIM) devices. Current interconnect technology employs a Cu damascene process. To prevent its migration into the surrounding materials, a cladding diffusion barrier is required for all Cu lines. As metal interconnect lines continue to shrink, the contribution of the cladding barrier to the overall resistivity (ρ) of the lines increases. A commonly used Cu diffusion barrier, TiN, has a ρ of approximately 100 $\mu\Omega$ cm. Ru has a much lower bulk resistivity (ρ_0) of ~7.1–7.8 $\mu\Omega$ cm,[1–3] low solid solubility in Cu, strong adhesion to Cu, high melting temperature, is relatively easy to etch, and can be used as a seed layer for Cu electroplating, making it an attractive alternative barrier metal.[1,4,5] As interconnect trace dimensions shrink well below the bulk electron mean free path (λ_{mp}) of Cu (~39 nm), the overall line ρ of Cu lines increases significantly due to increased scattering.[6] At these small line dimensions (<10 nm), surface scattering becomes dominant, and the effective mean free path ($\lambda_{mp,eff}$) falls below that of the bulk value so that the product of ρ_0 and λ_{mp} becomes a better proxy for the performance of a thin metal line.[1] Metals with shorter λ_{mp} do not experience as drastic an increase in ρ with decreasing dimensions as do metals with longer λ_{mp}. λ_{mp} of Ru (6.6 nm) is much shorter than λ_{mp} of Cu. In addition, Ru does not require a barrier layer. Thus, despite its higher overall ρ_0, Ru becomes an attractive replacement for Cu for future ultranarrow interconnects.[7,8] Finally, in the front end of the line, the relatively high reported work functions (Φ_M) of

sputter deposited Ru (>4.7 eV) and RuO_2 (5.0–5.2 eV) make them attractive as gate electrodes for pMOS transistors or MIM capacitors where a high Φ_M can help to reduce threshold voltage and minimize leakage currents.[9–13]

All of these applications require the controlled deposition of thin, uniform, and conformal Ru films. Atomic layer deposition (ALD), due to purge-separated dosing of precursors and self-saturating surface reactions, offers inherent atomic scale thickness control, high uniformity, and high conformality at relatively low temperatures (<300 °C). Because of these advantages, interest in depositing pure metallic thin films via ALD has grown tremendously in recent years and, in particular, ALD processes for Ru are strongly desired.[14] Although a number of ALD processes for Ru have been reported, most employ nonzero oxidation state precursors, such as $Ru(EtCp)_2$, which are typically characterized by long nucleation delays of up to 200 or more ALD cycles prior to the film growth.[15–17] Long nucleation delays are undesirable not only due to increased process time but also slow nucleation can lead to island-like growth, which, in turn, can result in increased roughness. Since targeted applications of Ru films are generally only a few to tens of nanometers thick, nucleation delay is a critical growth parameter. Other work has shown that zero oxidation state Ru precursors can significantly reduce nucleation delays for O_2-based thermal ALD processes.[18–23] Efforts have also been made to improve the quality of as-deposited films using "ABC" type processes such as adding an H_2 pulse in addition to the precursor and O_2 pulses.[24] However, ρ of these films are generally in the range of 18–40 $\mu\Omega$ cm, well above bulk Ru. Austin *et al.* reported a zero oxidation state ALD Ru process, based on η^4-2,3-dimethylbutadiene ruthenium tricarbonyl [$Ru(DMBD)(CO)_3$] and O_2, which shows zero nucleation delay, a Ru density of 12.2 g/cm^3, surface roughness of ~0.6 nm RMS, and as-deposited ρ as low as 14 $\mu\Omega$ cm.[25,26] Gao *et al.* later reported a ρ of 39 $\mu\Omega$ cm for an $Ru(DMBD)(CO)_3$ process using H_2O as a coreactant.[27] While the $Ru(DMBD)(CO)_3/O_2$ process has among the lowest ρ values reported for ALD Ru (see Table I), it is still significantly greater than ρ_0 of the pure bulk Ru metal.[25,26]

In this work, we investigate the impact of elevated temperature postdeposition annealing in both pure N_2 and H_2/N_2 forming gas environments on the morphology, composition, and ρ as a function of the thickness of ALD Ru films deposited using $Ru(DMBD)(CO)_3$ and O_2. We also report the effective work function ($\Phi_{M,eff}$) of ALD Ru on ALD Al_2O_3 and HfO_2 extracted from a series of MOS capacitors and direct measurement of the electron energy barrier height (φ_{Bn}) at the Ru/Al_2O_3 and Ru/HfO_2 interfaces in MIM capacitors using internal photoemission (IPE) spectroscopy.

II. EXPERIMENT

ALD of Ru thin films was performed in a Picosun SUNALE R-200 reactor at 260 °C using 99.999 99% N_2 purge separated pulses of $Ru(DMBD)(CO)_3$ and O_2. The deposition chamber was operated at a pressure of 2 Torr with a constant flow of N_2 into which the dosing pulses were introduced. $Ru(DMBD)(CO)_3$ was heated to 52 °C and delivered with N_2 assist using a PicoSolid Booster. A 1.5 s $Ru(DMBD)(CO)_3$/30 s N_2/2.5 s O_2/30 s N_2 pulse sequence was used, which produced a growth per cycle (GPC) of approximately 0.05 nm/cycle.

TABLE I. Resistivity values for representative ALD and CVD Ru thin films.

Process	Precursor	Precursor	ρ ($\mu\Omega$ cm)	Reference
ALD	$Ru(DBMD)(CO)_3$	H_2O	39	27
	IMBCHDRu	O_2	30	19
	(HD)PrMePhRu	O_2	29–36	18
	EBBDRu	O_2	26	22
	EBBDRu	O_2, H_2	26	24
	ECPR	O_2	22–26	35
	$Ru(C_9H_{13})_2$	O_2	20	36
	EBECHRu	O_2	20	21
	DMPR	O_2	18–24	37
	EBCHDRu	O_2	18	20
	$Ru(DMPD)_2$	N_2 plasma	17	38
	$Ru(Cp)(Co)_2Et$	O_2 and O_2 plasma	16	39
	$Ru(thd)_3$	O_2	15–20	17
	$Ru(EtCp)_2$	O_2	15	15
	$Ru(DBMD)(CO)_3$	O_2	14	25,34
	$Ru(Cp)_2$	O_2 (air)	13	16
	EBECHRu	O_2	11[a]	40
	$Ru(chd)_2$	O_2	10–16	23
	$Ru(DBMD)(CO)_3$	O_2	9.1[a]	This work
CVD	$Ru(EtCp)_2$		20–30	41
	$Ru_3(CO)_{12}$		16.9	42
	$Ru(C_5H_5)_2$		14.8	42
Bulk Ru	—	—	7.1–7.8	1–3

[a]Following postdeposition anneal.

Thermal stability studies (see the Appendix) were performed on $Ru(DMBD)(CO)_3$ samples prepared without solvent under an N_2 atmosphere in standard J-Young type NMR tubes. Tubes were subsequently heated in a hot water bath and held at constant temperatures of 45 and 60 °C. At intervals of 1, 2, 3, 4, and 8 weeks, the samples were pulled from the bath, allowed to cool to room temperature, inspected visually, analyzed using proton nuclear magnetic resonance (^{1}H NMR), and then returned to the warm bath at their respective temperature. ^{1}H NMR spectra were collected at 500 MHz on an Agilent ProPulse spectrometer equipped with a 5 mm PFG OneNMR probe operated by software VNMRJ 4.2.

Isochronal postdeposition anneals were performed in a quartz tube furnace at a pressure of approximately 1 Torr in either 99.999% N_2 or a 99.999% pure 3% H_2/97% N_2 forming gas at 400, 450, or 500 °C. Samples were characterized at 20 min intervals. To assess ρ, Ru films were deposited on 800 nm of thermally grown SiO_2 on Si and measured using a Jandel RM2 4-pt probe. Surface roughness was measured with an Asylum MFP-3D atomic force microscope (AFM) using an Al coated Si cantilever tip in the tapping mode. Crystallinity and grain size were determined grazing incidence x-ray diffraction (GIXRD), carried out at an incidence of 0.7°. The film thickness was determined using x-ray reflectometry (XRR). Both XRD and XRR measurements were made using a Rigaku Ultima IV diffractometer with Cu Kα radiation (λ = 1.5406 Å).

The oxide film thickness and Ru film thicknesses below 20 nm were also measured using a J. A. Woollam M-2000 variable angle spectroscopic ellipsometer (VASE) in the wavelength range of 300–1000 nm. The data were fit using a Cody–Lorentz model for Ru and a Cauchy model for oxides. Secondary ion mass spectrometry (SIMS) depth profiling was carried out by EAG Laboratories using Physical Electronics 6650 Dynamic Secondary Ion Mass Spectrometry (Phi-6650) with a quadrupole spectrometer. The primary ion beam, energy, and current were Cs, 2 keV, and 100 nA, respectively.

$\Phi_{M,eff}$ of Ru was determined using a series of $Ru/Al_2O_3/Si$ and $Ru/HfO_2/Si$ metal/oxide/semiconductor (MOS) capacitors. Al_2O_3 and HfO_2 were deposited via ALD in a Picosun R-150 reactor. The R-150 deposition chamber was also operated at a pressure of 2 Torr with a constant flow of N_2 into which the dosing pulses were introduced. Al_2O_3 films were deposited at 300 °C using trimethylaluminum (TMA) and H_2O. HfO_2 films were deposited at 350 °C using bis(methylcyclopentadienyl)methoxymethyl hafnium and H_2O.[28] Immediately prior to ALD, p-type Si substrates (10^{15} cm^{-3} boron doped) from SUMCO were prepared using an RCA cleaning procedure consisting of (i) soak in a 1:10 bath of HF and H_2O for 10 min, (ii) rinse in pure deionized (DI) H_2O, (iii) soak in a 75 °C bath of NH_4OH, H_2O_2 and H_2O at 1:1:5 concentration for 15 min, (iv) rinse in DI, (v) soak in a 75 °C bath of 1:1:6 of HCl, H_2O_2, and H_2O for 15 min, and (vi) final rinse in DI. HF, NH_4OH, HCl, and H_2O_2 were acquired from KMG and are semiconductor grade with impurity levels of less than 10 ppb for most trace metals. This cleaning process chemically oxidizes the Si surface, resulting in the formation of an approximately 3.5 nm thick layer of SiO_2. Following Al_2O_3 or HfO_2 deposition, 50 nm of Ru was deposited via ALD to form the top electrode. MOS capacitor formation was completed by forming circular Ru top electrodes ranging in diameter from 63 to 250 μm. Ru films were coated with Microposit S1813 positive photoresist (PR) and then patterned via photolithography. Following PR patterning, Ru was etched in an Oxford Instruments PlasmaPro 100 Cobra inductively coupled plasma etcher using a 1500 W plasma composed of 90% oxygen and 10% chlorine at 30 mTorr. At a substrate bias of 100 W with the substrate held at 20 °C, the etch rate was 75 nm/min. Capacitance versus voltage (CV) measurements were performed in a dark box using a probe station and an Agilent 4284A LCR meter. Current versus voltage (I–V) measurements were performed using an Agilent 4155 Semiconductor Parameter Analyzer.

IPE spectroscopy measurements were conducted on MIM devices with a home-built system using UV light from a 150W Xe arc lamp source that was passed through a monochromator and then a long-pass filter (to remove second-order diffraction) before being focused on the device. MIM devices consisted of Ru/insulator/TaN/Ta/SiO_2/Si stacks with a 12 nm thick Ru electrode and 10 nm of either HfO_2 or Al_2O_3 as the insulator. TaN bottom electrode substrates planarized by chemical mechanical polishing were provided by ON Semiconductor. Electrical bias was applied to the TaN bottom electrode and the Ru top electrode was held at the ground. At each applied voltage bias, the electrical current was measured as the photon energy ($h\nu$) was swept from 2 to 5 eV (620–248 nm). The quantum yield, Y, was calculated from the normalized current. IPE spectral thresholds, φ_{thresh}—the photon energy at which photo-induced current exceeds the dark current for a given applied bias—were determined from plots of $Y^{1/2}$ versus $h\nu$.[29,30] The zero-field barrier height, φ_{Bn}, for the Ru/insulator interface was then determined by taking the y-intercept of a Schottky plot of φ_{thresh} versus the square root of the insulator electric field, $\xi_{ox}^{1/2}$, with an estimated accuracy of ±0.1 eV.[31] Further details about the system and barrier analysis may be found in our earlier work using the same IPE system.[32,33]

III. RESULTS AND DISCUSSION

A. Resistivity

Shown in Fig. 1 is a plot of the average ρ versus anneal time for 30 nm thick ALD Ru films annealed at 400, 450, and 500 °C in either N_2 or 3% H_2/N_2. After each 20 min anneal increment, ρ was measured and the samples were returned to the furnace for further annealing up to a total of 60 min. (Note that samples annealed for 60 min without interruption produced the same result as three sequential 20 min anneals.) For the Ru films annealed in pure N_2, the initial 20 min of annealing produced a similar 15% drop in ρ for all three temperatures, from around 16.1 $\mu\Omega$ cm as deposited to 13.7 $\mu\Omega$ cm following anneal.[34] Subsequent annealing for additional time at a given temperature had no significant additional impact on ρ for any of the temperatures investigated.

Annealing in 3% H_2 in N_2 produced a greater reduction in ρ as compared to the N_2 only annealed samples. In addition, the reduction in ρ was temperature dependent, being greatest at 500 °C and smallest at 400 °C with the improvement at 500 °C only slightly greater than at 450 °C. Subsequent annealing for longer times yielded additional gradual reductions in ρ. The lowest ρ of 9.1 $\mu\Omega$ cm is obtained after the 60 min anneal at 500 °C. As seen in Table I, this is among the lowest obtained for thin film Ru and approaches that of bulk Ru.

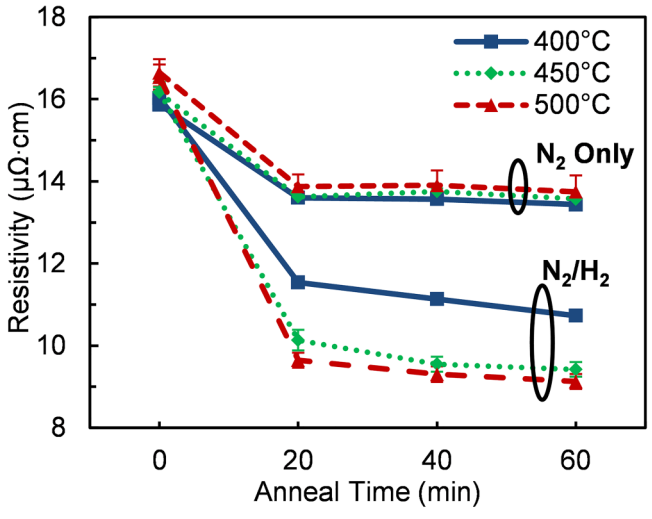

FIG. 1. Plot of the 30 nm thick Ru film ρ vs cumulative anneal time in either an N_2 or a H_2/N_2 ambient at various temperatures.

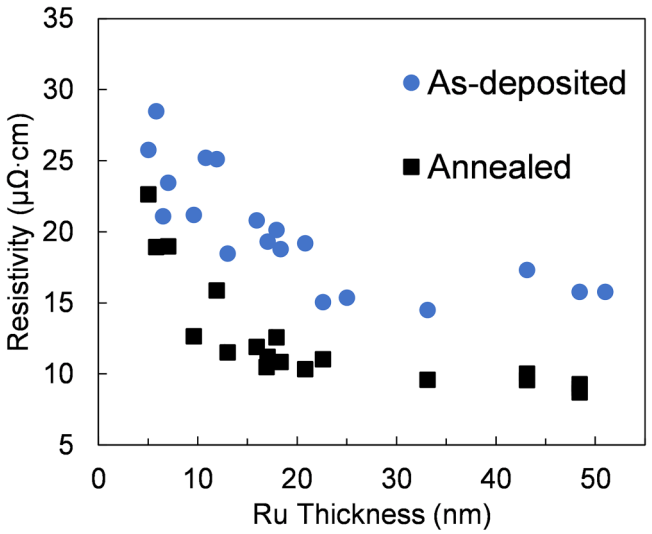

FIG. 2. Plot of ρ vs thickness for Ru films either as-deposited (blue circles) or following postannealing for 60 min at 500 °C in H_2/N_2 (black squares).

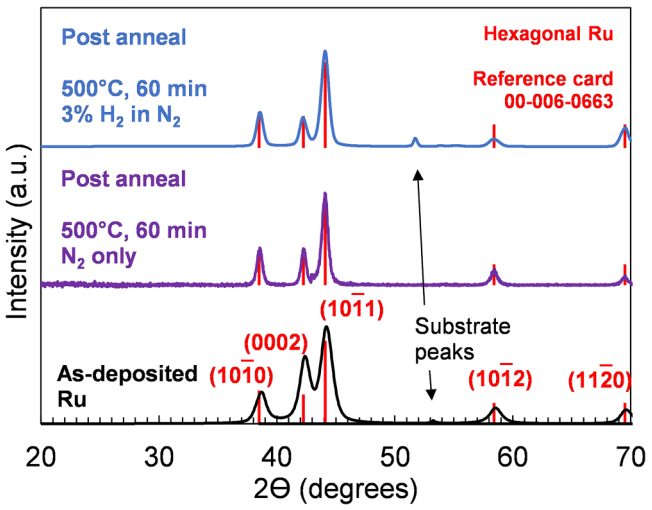

FIG. 3. GIXRD spectra of a 25 nm thick ALD Ru film as-deposited and postannealing for 60 min at 500 °C in either N_2 or H_2/N_2.

Shown in Fig. 2 is a plot of ρ versus thickness for ALD Ru films deposited on SiO_2, both as-deposited and after a 60 min anneal at 500 °C in 3% H_2/N_2. For all thicknesses, ρ was reduced by annealing. For Ru films thicker than about 30 nm, ρ was roughly independent of thickness with the lowest ρ of 13.4 $\mu\Omega$ cm for as-deposited films with an average ρ of 15.9 $\mu\Omega$ cm and a standard deviation of 1.5 $\mu\Omega$ cm. For annealed films, the lowest ρ was 9.1 $\mu\Omega$ cm and an average ρ of 9.4 $\mu\Omega$ cm with a standard deviation of 0.4 $\mu\Omega$ cm.

Below about 25 nm for as-deposited films and around 15 nm for the annealed films, ρ_{Ru} increases with decreasing film thickness. It is well known that the resistivity of metals lines increases as dimensions shrink and that resistivity is dominated by surface and grain scattering.[1] For metals with a spherical Fermi surface such as Cu, simplistic modeling of the resistivity of a single crystalline film as a function of thickness may be performed using the Fuchs–Sondheimer model. However, for metals such Ru having a nonspherical Fermi surface, modeling a polycrystalline thin film becomes more complex and is beyond the scope of the present work.[1,2,43–45]

B. Structural properties

Crystallographic and surface properties were examined with GIXRD and AFM. Shown in Fig. 3 are GIXRD spectra of a 25 nm thick ALD Ru film on 800 nm of SiO_2, as-deposited and postannealing for 60 min at 500 °C in either N_2 or H_2/N_2. The observed diffraction peaks for both the as-deposited and postannealed films correspond to polycrystalline hexagonal Ru. As-deposited and postannealed films appeared free of any significant RuO_2 crystallites as there was no indication of the strong RuO_2 (111) or (200) peaks, which would be expected at 31° and 37°, respectively. In order to better gauge the relative intensities and widths of the crystalline plane reflections, all spectra were normalized to the Ru (10$\bar{1}$1) peak. From a Scherrer analysis of the peak widths, we estimate an average Ru crystallite size of approximately 6 nm for the as-deposited sample increasing to approximately 15 nm following annealing in either N_2 or H_2/N_2.

Comparison of the relative peak intensities in the as-deposited film to that of a powder diffraction reference shows a slightly higher reflection intensity for the (0002) peak compared to the annealed samples. Following 500 °C annealing in either N_2 or H_2/N_2, the relative intensity of the (0002) peak becomes closer to what would be expected for randomized crystallites. In order to determine if the apparently increased intensity of the (0002) peak is a result of it resting on the broader (10$\bar{1}$1) peak in the as-deposited film or whether it is due to a crystallite orientation preference, omega scans were taken for both conditions with 2θ fixed to the (0002) reflection angle. This data revealed no preferred orientation normal to the surface as-deposited. Similar omega scans of other crystallite orientations yielded similar results.

Figure 4 shows AFM micrographs from a 46 nm thick Ru film as-deposited and postannealed at 500 °C for 60 min in either N_2 or H_2/N_2. Surface roughness in the as-deposited film was found to be 0.7 nm RMS with a 6 nm peak-to-valley range. Following the 500 °C N_2 anneal, the roughness increased to 2.3 nm RMS with a 30 nm peak-to-valley. The peak-to-valley range increase is due to the growth of small spires on the surface of the annealed sample. A similar increase in roughness was observed for the H_2/N_2 annealed film to 2.1 nm RMS with a 27 nm peak-to-valley. This increase in roughness suggests an increase in the crystallite size and corroborates the XRD results in Fig. 3.

Potential mechanisms for the ρ improvement observed in the annealed films (Figs. 1 and 2) include (i) crystal grain growth/consolidation and a reduction of grain boundaries, (ii) out-gassing/elimination of residual carbon or hydrogen impurities, or (iii) dissociation of any residual oxygen remaining in the film. For a 21 nm

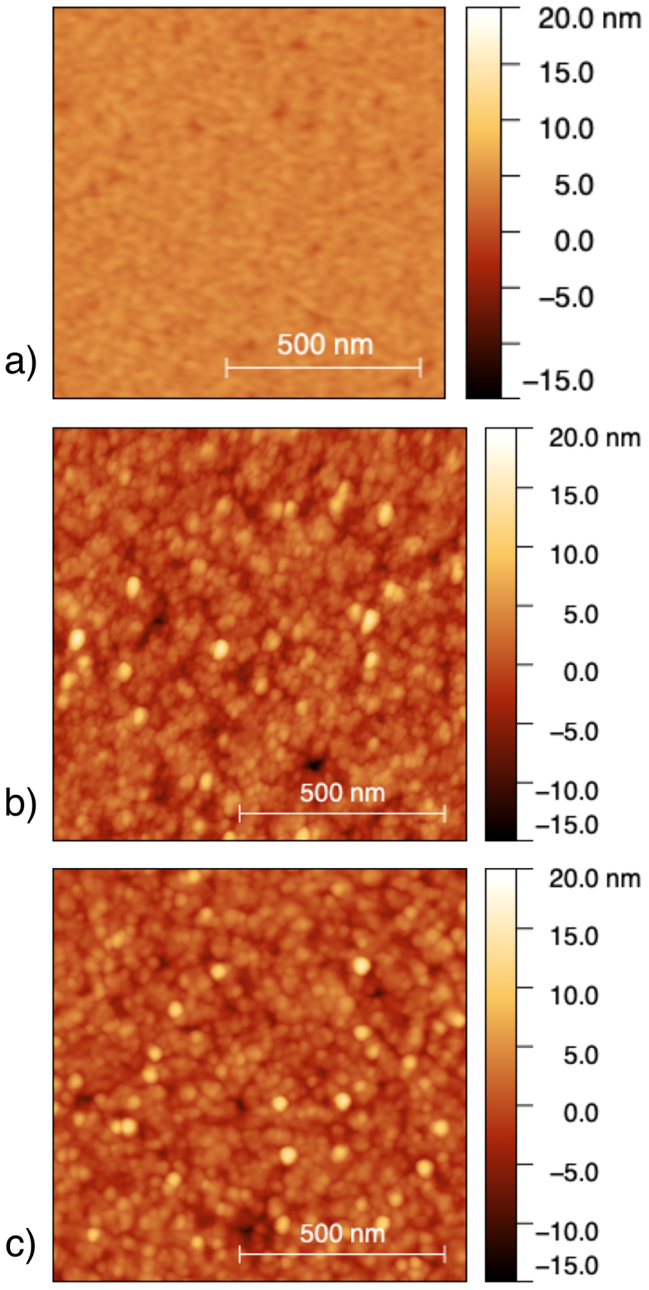

FIG. 4. AFM micrographs showing surface morphology of representative 46 nm thick Ru films (a) as-deposited and following annealing at 500 °C for 60 min in either (b) N_2 or (c) H_2/N_2.

thick Ru film deposited using alternating pulses of (ethylbenzyl)(1-ethyl-1,4-cyclohexadienyl)Ru(0) (EBECHRu) and O_2 at 325 °C (*above* the decomposition temperature of EBECHRu), Popovici *et al.* reported an as-deposited ρ of ~15 μΩ cm, which was reduced to ~11 μΩ cm after annealing for 20 min at 420 °C in H_2/N_2 forming gas, which they attributed to the grain growth.[40] Overall, GIXRD and AFM show that annealing in either N_2 or H_2/N_2 results in similar growth of the randomly oriented hexagonal Ru crystallites, indicating that reduced grain boundary scattering does play a role in the reduction of ρ observed following annealing in either anneal gas. However, as there were no significant differences in film morphology between the two gasses, morphology alone cannot explain the additional dependence on anneal gas seen in the present work, with the H_2/N_2 showing greater improvement in ρ than N_2. This suggests that a difference in the impurity content following the anneals likely also plays a role.

C. Composition

To assess the carbon, oxygen, and hydrogen content, SIMS depth profiles are shown in Fig. 5 for 45–50 nm thick ALD Ru films on SiO_2/Si (a) as-deposited or following 60 min 500 °C annealing in either (b) N_2 or (c) H_2/N_2. Ru and Si were not quantified and are shown only for film depth reference. In the as-deposited films, SIMS indicates below surface concentrations of carbon, oxygen, and hydrogen of approximately 9×10^{20}, $2–3 \times 10^{20}$, and 2×10^{19} atoms/cm^3, respectively. Annealing in N_2 results in a reduction in carbon concentration to approximately $0.8–1 \times 10^{20}$ while both oxygen and hydrogen concentration remained relatively unchanged. Annealing instead in H_2/N_2 results in an additional reduction in carbon as well as reductions in oxygen and hydrogen concentration as well to approximately 3×10^{19}, $0.6–1 \times 10^{20}$, and 5×10^{18} atoms/cm^3, respectively. In the H_2/N_2 annealed Ru film, the concentration of both O and C increases as a function of depth into the film, suggesting that annealing for longer than 60 min or at a higher temperature might further reduce the carbon and oxygen content in the bulk of the film. A continued slight reduction of O and C in the depth of the film could explain the small additional reduction in resistivity as the duration of the H_2/N_2 anneal is increased from 20 to 60 min and as the temperature is increased from 450 to 500 °C (Fig. 1). Note that due to ambient exposure prior to SIMS, all three samples show an increased concentration of C, O, and H impurities at the surface. For the as-deposited and H_2/N_2 annealed samples, the concentration of C and H drops sharply away from the interface. In the N_2 annealed sample, the increased surface concentration of C and H extends more deeply into the film to about 5 nm before dropping below the C concentration in the as-deposited sample and to about 13 nm before dropping to the as-deposited concentration of H. Since annealing in either gas results in nearly the same average crystallite size and RMS roughness, it is likely that lower ρ produced by H_2/N_2 versus N_2 anneal is due to the lower residual concentrations of C, O, and H. The N_2/H_2 anneal likely reduces any remaining RuO_x in the film and in the process drives off residual hydrogen and carbon,[46] processes which do not appear to take place under vacuum or N_2 annealing.[47]

D. Work function and barrier height

Knowledge of metal/oxide and metal/semiconductor interface electron barrier heights (φ_{bn}) and effective metal work functions is necessary for predicting and optimizing device operation, particularly, for transistor gate electrodes, MIM diodes, and MIM

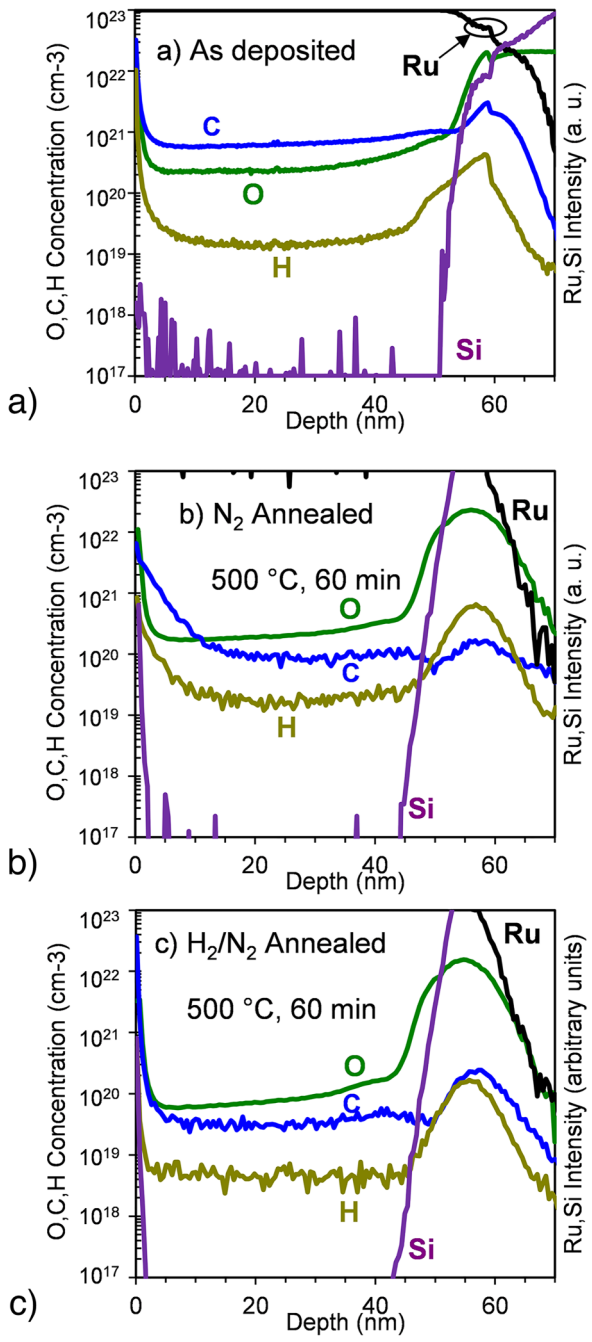

FIG. 5. SIMS depth profile of ALD Ru thin films (a) as-deposited and after post-60 min 500 °C annealing in either (b) N_2 or (c) H_2/N_2.

capacitors.[47] In the ideal Schottky–Mott relationship, φ_{bn} should vary with the vacuum work function of the metal ($\Phi_{M,vac}$) and the electron affinity of the oxide (χ_i) so that $\varphi_{bn} = \Phi_{M,vac} - \chi_i$. In practice, however, this simple model often does not hold due to strongly process dependent nonidealities such as deep level defects/trapped charge at the metal–dielectric interface or in the dielectric near the interface, unintended (or intended) interfacial layers, and deposition method of the metal. To account for differences between the Schottky–Mott prediction and actual barrier height, a metal may be considered to exhibit $\Phi_{M,eff}$, which is dependent upon the specific oxide with which it is in contact.

To determine $\Phi_{M,eff}$, measurements were made on a series of $Ru/Al_2O_3/p\text{-}Si$ and $Ru/HfO_2/p\text{-}Si$ MOS capacitors with 10, 20, 30, and 40 nm thick oxides. Several capacitor areas were measured for each oxide thickness. The accumulation, or oxide capacitance, C_{ox}, was calculated from the x-intercept of the linear regime of a plot of $(dC/dV)^{1/2}$ versus measured capacitance at each voltage. The x-intercept of a $(C_{ox}/C)^2$ versus V plot was then used to calculate the shift in flat band voltage from ideal, ΔV_{FB}.[48] V_{FB} for each device was then determined by adding ΔV_{FB} to the calculated ideal flatband voltage, $V_{FB,ideal}$. Shown in Fig. 6, V_{FB} is plotted versus equivalent dielectric thickness ($EOT = dox \cdot \kappa_{SiO_2}/\kappa_{oxide}$) for the $Ru/Al_2O_3/p\text{-}Si$ and $Ru/HfO_2/p\text{-}Si$ MOS capacitors following a 60 min 500 °C anneal in H_2/N_2. Assuming that charge at the interface is independent of oxide thickness, linear extrapolation to the y-axis yields the metal–semiconductor work function difference, $\Delta\Phi_{MS,eff} = \Phi_{M,eff} - \Phi_S$ for each capacitor type, where the silicon work function, Φ_S, is determined from the doping density.[49,50] $\Phi_{Ru,eff}$ was found to be 4.9 eV for the Al_2O_3 devices and 5.3 eV for the HfO_2 devices.

To date, $\Phi_{M,eff}$ values for Ru barriers have been reported only for samples that have undergone postdeposition and postmetallization anneals. Previous reports of $\Phi_{M,eff}$ for Ru are summarized in Table II. The value of $\Phi_{Ru,eff}$ on Al_2O_3 calculated here is close to the 4.98 eV reported for metal-organic chemical vapor deposited (MOCVD) Ru on ALD Al_2O_3.[13] In that work, the Al_2O_3 was annealed for 30 min at 420 °C in 10% H_2 and 90% N_2 prior to Ru deposition. In this work,

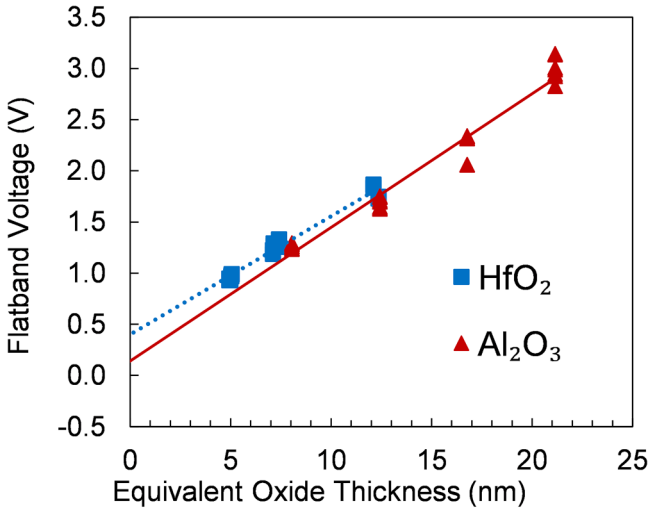

FIG. 6. V_{FB} vs EOT for MOS capacitors with HfO_2 and Al_2O_3 dielectrics following a 60 min, 500 °C anneal in H_2/N_2.

annealing was performed post-Ru deposition for 60 min in 3% H_2 and 97% N_2. The difference in deposition method and anneal treatment, and the potential difference in residual oxygen in Ru likely account for the difference in $\Phi_{Ru,eff}$. The value of $\Phi_{Ru,eff}$ on HfO_2 found here is in general agreement with values of 5.1 and 5.3 eV reported for Ru/HfO_2 capacitors in which Ru was deposited via digital CVD and MOCVD, respectively.[51,52]

The technique used above for MOS devices is not viable for determining $\Phi_{M,eff}$ on MIM devices because the CV output characteristics do not exhibit a V_{FB}. Instead, IPE spectroscopy was used to directly determine φ_{Bn}. Shown in Fig. 7 are representative Schottky plots of IPE φ_{thresh} versus $\xi_{ox}^{1/2}$, for electron emission from the Ru top electrode of (a) Ru/Al_2O_3/TaN and (b) Ru/HfO_2/TaN MIM capacitors. The zero-field barrier height between the Ru Fermi level and the Al_2O_3 conduction band edge, $\varphi_{Bn,Ru/Al_2O_3}$, for as-deposited and devices annealed for 60 min at 500 °C in H_2/N_2 was determined to be 3.6 ± 0.1 and 3.4 ± 0.1 eV, respectively. Note that we also measured $\varphi_{Bn,Ru/Al_2O_3} = 3.6 \pm 0.1$ eV for as-deposited Ru/Al_2O_3/TiN MIM and Ru/Al_2O_3/Si MOS devices. Assuming $\chi_{Al_2O_3} = 1.4$ eV,[53] $\Phi_{Ru,eff(IPE)}$ would be approximately 4.8 ± 0.1 eV following the 500 °C H_2/N_2 anneal. This is consistent with the estimate of 4.9 eV obtained from Fig. 6 as well as a previous report of 4.98 eV determined using the V_{FB} versus insulator thickness method for annealed MOCVD Ru on annealed ALD Al_2O_3.[13]

For the Ru/HfO_2/TaN devices in Fig. 7(b), the as-deposited devices yielded $\varphi_{bn\text{-}Ru/HfO_2} \simeq 3.8 \pm 0.1$ eV. Following annealing, $\varphi_{bn\text{-}Ru/HfO_2}$ was also found to be $\simeq 3.8 \pm 0.1$ eV, essentially unchanged within experimental error. Assuming $\chi_{HfO_2} = 2.0$ eV,[11] this yields an $\Phi_{Ru,eff}$ of roughly 5.8 eV, much larger than expected from the difference of $\Phi_{Ru,vac}$ and χ_{HfO_2}. This could be due to the presence of a negative dipole at the Ru/HfO_2 interface, which has been reported in previous work,[47] and/or the presence of a RuO_2 interfacial layer at the Ru/HfO_2 interface.[46] In our prior work, HfO_2 and Al_2O_3 have been shown to have similar barrier heights when in contact with the same metal, believed to be due to charging and dipoles at the interface.[32,33] Here, however, $\varphi_{bn\text{-}Ru/HfO_2}$ was about 0.4 eV larger than $\varphi_{bn\text{-}Ru/Al_2O_3}$. The larger Ru barrier height for HfO_2 as compared to Al_2O_3 is in good agreement with $\Phi_{M,eff}$ measurements in Fig. 6, as well as those reported in the literature (see Table II). To understand this, it is necessary to consider how each dielectric will interact with Ru and the interface that will result from this interaction. In the case of the Al_2O_3/Ru interface, due to the high oxygen affinity of Al as compared to Ru, Ru should

TABLE II. Effective work function values of Ru deposited via various methods on various oxides.

Ru deposition method	Insulator	$\Phi_{Ru,eff}$ (eV)	Reference
Evaporation	Vacuum	4.7	54
MOCVD	Al_2O_3	4.98	13
MOCVD	HfO_2	5.3	51
Sputtering	HfO_2	5	56
Digital CVD	HfO_2	5.1	52
MOCVD	SiO_2	5.3	13
ALD	SiO_2	4.8	55

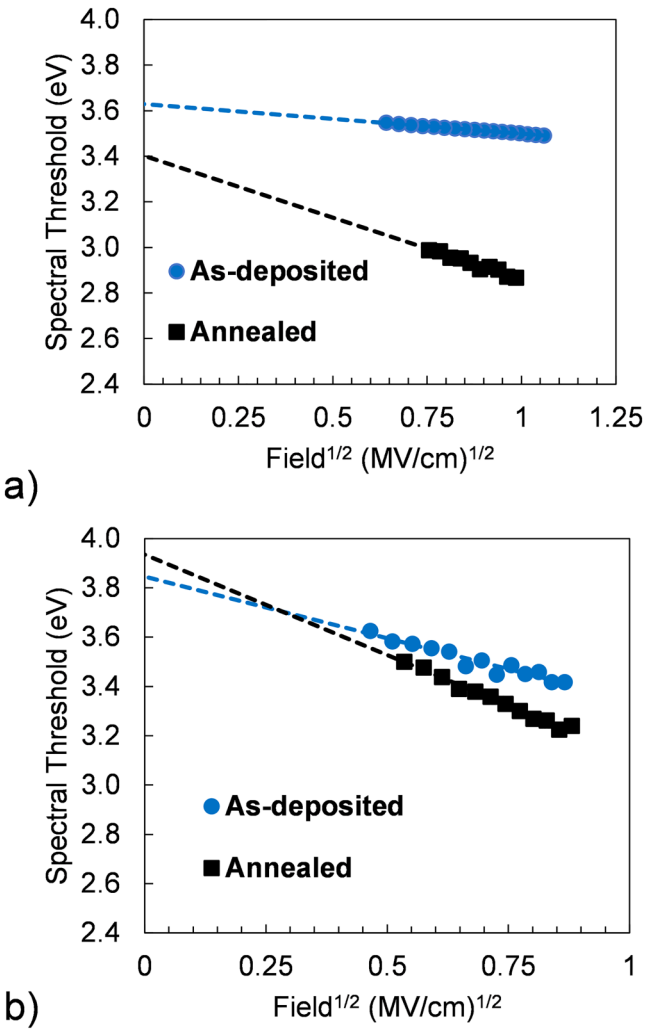

FIG. 7. Schottky plots of IPE φ_{thresh} vs $\xi_{ox}^{1/2}$ for (a) Ru/Al_2O_3/TaN and (b) Ru/HfO_2/TaN MIM capacitors following a 60 min anneal at 500 °C in H_2/N_2.

experience less oxidation than for the HfO_2 interface, where the comparatively lower oxygen affinity of Hf will result in greater oxidation of Ru. As RuO_2 has a larger work function than Ru, 5.0–5.2 eV vs 4.7–5.3 eV, respectively,[11–13,46,51,52,54–56] greater RuO_x formation at the HfO_2/Ru interface would lead to a larger extracted effective work function than for the Al_2O_3/Ru device.

For Al_2O_3, the IPE measured $\varphi_{bn\text{-}Ru/Al_2O_3}$ decreased by 0.2 eV after PMA to 3.4 eV. Previous work with sputtered Ru electrodes on MOS devices showed that PMA in a forming gas as compared to an oxygen environment led to a dipole at the Ru-insulator interface that resulted in a decrease of the Ru barrier height with both HfO_2 and SiO_2.[46,47] It was postulated that the reduction of the barrier height following the forming gas anneal was due either to a reduction of RuO_x or to hydroxyl formation at the interface.[46] The

decrease in $\varphi_{bn\text{-}Ru/Al_2O_3}$ following forming gas anneal could thus be due to the reduction of any interfacial RuO_x that forms in contact with Al_2O_3. However, $\varphi_{bn\text{-}Ru/HfO_2}$ did not change following PMA, remaining within experimental error of ±0.1 eV, at about 3.85 eV. One possible explanation as to why HfO_2 does not exhibit the same φ_{bn-Ru} decrease that is seen for Al_2O_3 is that the 500 °C forming gas anneal was not sufficient to entirely reduce the RuO_x interfacial layer on the HfO_2 sample.

While the Ru barrier heights showed either no change or a slight reduction following anneal, depending on the insulator, there was a distinct change in the slope of the Schottky plots for both insulators, most dramatically for the Al_2O_3/Ru interface. Ideally, the slope of the Schottky plot should be proportional to the dielectric constant of the insulator in question, assuming a single metal work function. This is often not the case as the field induced barrier lowering (but not φ_{bn}) is impacted by interfacial layers, charge in the oxide, and also lateral nonuniformity of the metal work function, in the case of Ru.[47] The increased slope of the Schottky plots for both Ru barriers could indicate an increased degree of lateral nonuniformity in the Ru work function.

IV. SUMMARY/CONCLUSIONS

The electrical properties, morphology, and composition of Ru deposited by thermal ALD using $Ru(DMBD)(CO)_3$ and O_2 were investigated before and after annealing at up to 500 °C in either N_2 or H_2/N_2. GIXRD and omega XRD scans of as-deposited films indicate randomly oriented polycrystalline hexagonal Ru with an estimated average crystallite size of ~6.3 nm. Polycrystalline RuO_2 was not detected. The average resistivity, ρ, of as-deposited films thicker than 30 nm was approximately 16 $\mu\Omega$ cm, increasing with decreasing thickness for films thinner than about 30 nm. Annealing for 20 min in N_2 at 400 °C reduced ρ to an average of 13.7 $\mu\Omega$ cm with no significant additional drop in ρ for increased temperature up to 500 °C or time up to 60 min. Annealing in H_2/N_2 gas produced a lower average ρ with the best results obtained after 60 min at 500 °C, which yielded an average ρ of 9.4 $\mu\Omega$ cm, approaching that of bulk Ru (7.1–7.8 $\mu\Omega$ cm).

Since annealing in either gas resulted in nearly the same average crystallite size and RMS roughness, the lower resistivity produced by the H_2/N_2 anneal versus the N_2 anneal is likely due to the lower residual concentrations of C, O, and H in the H_2/N_2 annealed films, attributable to the reducing nature of the H_2/N_2 ambient. Using a series of MOS capacitors, the $\Phi_{M,eff}$ for H_2/N_2 annealed Ru on ALD-deposited Al_2O_3 was determined to be 4.9 eV, while $\Phi_{M,eff}$ on ALD-deposited HfO_2 was determined to be 5.3 eV. The difference in $\Phi_{M,eff}$ between the two insulators is consistent with direct IPE measurements of the φ_{Bn} between the Ru Fermi level and the Al_2O_3 or HfO_2 conduction band edge for MIM devices annealed for 60 min at 500 °C in H_2/N_2, determined to be 3.4 ± 0.1 and 3.8 ± 0.1 eV, respectively. The larger measured $\Phi_{M,eff}$ and φ_{Bn} on HfO_2 versus Al_2O_3 may be due to the presence of an RuO_x interfacial layer. Overall, the low ρ and large $\Phi_{M,eff}$ of ALD Ru deposited using $Ru(DMBD)(CO)_3$ and O_2 appears promising for microelectronics applications.

ACKNOWLEDGMENTS

The authors acknowledge EMD Performance Materials and Lam Research Corporation for partial financial support of this work, ON Semiconductor for TaN/Ta/SiO_2/Si substrates, Konner Holden (OSU) for assistance with AFM measurements, and Chris Tasker (OSU) for equipment support. This work was conducted at the Materials Synthesis and Characterization (MaSC) Center, a National Nanotechnology Coordinated Infrastructure (NNCI) Northwest Nanotechnology Infrastructure (NWNI) user facility at Oregon State University, which is supported, in part, by the National Science Foundation (Grant No. NNCI-2025489) and Oregon State University.

APPENDIX: Stability of $Ru(DMBD)(CO)_3$ under delivery conditions

ALD precursors containing carbonyl ligands are often regarded as having reduced thermal stability and lower decomposition temperature relative to those containing more robust and less easily displaced ligand types. Considering this, the suitability for ALD of such precursors is often questioned, as problems could arise with stability lifetime in the source vessel while heated to the evaporation temperature. Low thermal stability can also negatively affect the transport of vapor from the source vessel to the deposition chamber and, if insufficient, can lead to contamination or blockage of source lines, as well as malfunction of components such as pulsing valves. Furthermore, the upper limit of thermal stability typically marks the temperature beyond which the film growth mode begins to acquire a significant CVD-like character and may start to show loss of features representative of ALD, namely, self-limiting growth, thickness uniformity, and conformality. Although the saturating film growth temperature range has been described in detail in previous publications,[25,27,57] the stability of $Ru(DMBD)(CO)_3$ has recently been called into question.[27] In addition, the long term stability of $Ru(DMBD)(CO)_3$ at temperatures similar to those used in the source delivery system has not been reported before. To address this, we have performed a series of experiments where samples of $Ru(DMBD)(CO)_3$ have been continuously heated in N_2 at 45 and 60 °C for varying intervals of time up to eight weeks and examined for signs of decomposition by visual inspection and by ^{1}H NMR. Images of the samples prior to and after heating are shown in Fig. 8. A change in appearance from nearly colorless to pale yellow was observed upon heating which gradually intensified over the course of eight weeks to a golden-brown color. Analysis of the same samples by ^{1}H NMR revealed only those resonances originating from $Ru(DMBD)(CO)_3$ at chemical shifts of 1.92 ppm (s, 6H, CH_3), 1.45 ppm (d, 2H, CH_2), and 0.0 ppm (d, 2H, CH_2), plus one small unidentified impurity peak at 1.28 ppm, all of which were present in the original unheated sample. The integrated area of the impurity peak was compared to those of the precursor compound and was found to be consistent over the period of the experiment. This indicates that despite visual changes in the material, the composition of the material was not measurably changed. The NMR spectra can be found in Ref. 58. A summary of the results of the precursor's stability study can be found in Table III.

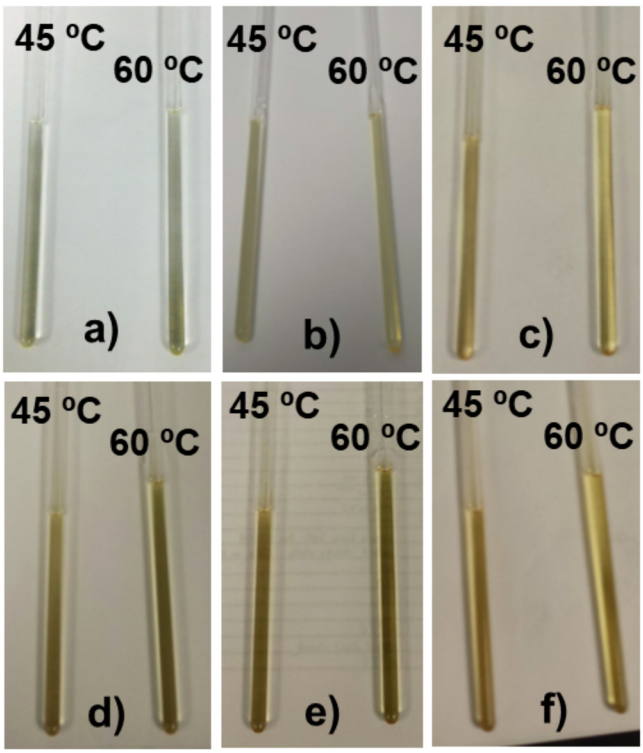

FIG. 8. Optical images of $Ru(DMDB)(CO)_3$ showing results of atmospheric stability study: (a) initial preheating and after (b) 1, (c) 2, (d) 3, (e) 4, and (f) 8 weeks at either 45 or 60 °C.

TABLE III. Summary of $Ru(DMBD)(CO)_3$ sample appearance and composition upon continuous heating at 45 and 60 °C at various time intervals up to eight weeks. Data with an asterisk (*) show a slight difference from other data due to rounding of peak integration.

	45 °C		60 °C	
Time	NMR purity (%)	Color	NMR purity (%)	Color
Initial (preheating)	97.5	Colorless/pale yellow and clear	97.5	Colorless/pale yellow and clear
1 week	97.5	Colorless/pale yellow and clear	97.5	Pale yellow and clear
2 weeks	97.5	Pale yellow and clear	97.4*	Pale yellow and clear
3 weeks	97.5	Pale yellow and clear	97.5	Pale yellow and clear
4 weeks	97.5	Pale yellow, slightly darker	97.5	Pale yellow, slightly darker
8 weeks	97.5	Pale yellow, slightly darker	97.5	Pale yellow, slightly darker

DATA AVAILABILITY

The data that support the findings of this study are available from the corresponding author upon reasonable request.

REFERENCES

[1]D. Gall, J. Appl. Phys. **119**, 085101 (2016).
[2]D. Gall, J. Appl. Phys. **127**, 050901 (2020).
[3]R. W. Powell, R. P. Tye, and M. J. Woodman, Platinum Met. Rev. **6**, 138 (1962).
[4]M. W. Lane, C. E. Murray, F. R. McFeely, P. M. Vereecken, and R. Rosenberg, Appl. Phys. Lett. **83**, 2330 (2003).
[5]K. Croes *et al.*, *2018 IEEE International Electron Devices Meeting (IEDM), San Francisco, CA, 1–5 December 2018* (IEEE, New York, 2018), pp. 5.3.1–5.3.4.
[6]I. Ciofi *et al.*, IEEE Trans. Electron Devices **63**, 2488 (2016).
[7]C.- Hu *et al.*, *2018 IEEE International Reliability Physics Symposium, IRPS, Burlingame, CA, 11–15 March 2018* (IEEE, New York, 2018), pp. 4F.1-1–4F.1-6.
[8]D. Gall, *2018 IEEE International Interconnect Technology Conference IITC, Santa Clara, CA, 4–7 June 2018* (IEEE, New York, 2018), pp. 157–159.
[9]J. H. Han, S. Han, W. Lee, S. W. Lee, S. K. Kim, J. Gatineau, C. Dussarrat, and C. S. Hwang, Appl. Phys. Lett. **99**, 022901 (2011).
[10]K. Frohlich *et al.*, ECS Trans. **50**, 79 (2013).
[11]H. Zhong, G. Heuss, and V. Misra, IEEE Electron Device Lett. **21**, 593 (2000).
[12]V. Misra and and H. Lazar, IEEE Electron Device Lett. **23**, 354 (2002).
[13]K. Fröhlich *et al.*, Mater. Sci. Eng. B **109**, 117 (2004).
[14]J. Hämäläinen, M. Ritala, and M. Leskelä, Chem. Mater. **26**, 786 (2014).
[15]S.-S. Yim, D.-J. Lee, K.-S. Kim, S.-H. Kim, T.-S. Yoon, and K.-B. Kim, J. Appl. Phys. **103**, 113509 (2008).
[16]T. Aaltonen, P. Alén, M. Ritala, and M. Leskelä, Chem. Vap. Depos. **9**, 45 (2003).
[17]T. Aaltonen, M. Ritala, K. Arstila, J. Keinonen, and M. Leskelä, Chem. Vap. Depos. **10**, 215 (2004).
[18]H. J. Jung, J. H. Han, E. A. Jung, B. K. Park, J.-H. Hwang, S. U. Son, C. G. Kim, T.-M. Chung, and K.-S. An, Chem. Mater. **26**, 7083 (2014).
[19]S.-H. Choi, T. Cheon, S.-H. Kim, D.-H. Kang, G.-S. Park, and S. Kim, J. Electrochem. Soc. **158**, D351 (2011).
[20]S. Yeo, S.-H. Choi, J.-Y. Park, S.-H. Kim, T. Cheon, B.-Y. Lim, and S. Kim, Thin Solid Films **546**, 2 (2013).
[21]T. E. Hong, S.-H. Choi, S. Yeo, J.-Y. Park, S.-H. Kim, T. Cheon, H. Kim, M.-K. Kim, and H. Kim, ECS J. Solid State Sci. Technol. **2**, P47 (2013).
[22]S. Yeo, J.-Y. Park, S.-J. Lee, D.-J. Lee, J. H. Seo, and S.-H. Kim, Microelectron. Eng. **137**, 16 (2015).
[23]J. M. Hwang *et al.*, J. Mater. Chem. C **9**, 3820 (2021).
[24]S. N. Chopra, M. F. J. Vos, M. A. Verheijen, J. G. Ekerdt, W. M. M. Kessels, and A. J. M. Mackus, J. Vac. Sci. Technol. A **38**, 062402 (2020).
[25]D. Z. Austin, M. A. Jenkins, D. Allman, S. Hose, D. Price, C. L. Dezelah, and John F. Conley, Jr., Chem. Mater. **29**, 1107 (2017).
[26]D. Z. Austin, M. A. Jenkins, D. Allman, S. Hose, D. Price, C. L. Dezelah, and J. F. Conley, Jr., Chem. Mater. **30**, 8983 (2018).
[27]Z. Gao, D. Le, A. Khaniya, C. L. Dezelah, J. Woodruff, R. K. Kanjolia, W. E. Kaden, T. S. Rahman, and P. Banerjee, Chem. Mater. **31**, 1304 (2019).
[28]C. L. Dezelah, J. Niinistö, K. Kukli, F. Munnik, J. Lu, M. Ritala, M. Leskelä, and L. Niinistö, Chem. Vap. Depos. **14**, 358 (2008).
[29]V. V. Afanas'ev and A. Stesmans, J. Appl. Phys. **102**, 081301 (2007).
[30]R. J. Powell, J. Appl. Phys. **41**, 2424 (1970).
[31]V. V. Afanas′ev, *Internal Photoemission Spectroscopy: Fundamentals and Recent Advances*, 2nd ed (Elsevier, London, 2014).
[32]M. A. Jenkins, J. M. McGlone, J. F. Wager, and J. F. Conley, Jr., J. Appl. Phys. **125**, 055301 (2019).
[33]M. A. Jenkins, T. Klarr, D. Z. Austin, W. Li, N. V. Nguyen, and J. F. Conley, Jr., Phys. Status Solidi RRL **12**, 1700437 (2018).

[34]M. H. Hayes, C. L. Dezelah, and J. F. Conley, Jr., ECS Trans. **85**, 743 (2018).
[35]M. Knaut, M. Junige, M. Albert, and J. W. Bartha, J. Vac. Sci. Technol. A **30**, 01A151 (2011).
[36]K. Gregorczyk, L. Henn-Lecordier, J. Gatineau, C. Dussarrat, and G. Rubloff, Chem. Mater. **23**, 2650 (2011).
[37]K. Kukli *et al.*, Thin Solid Films **520**, 2756 (2012).
[38]O. van der Straten, S. M. Rossnagel, J. P. Doyle, and K. P. Rodbell, ECS Trans. **1**, 51 (2006).
[39]N. Leick, R. O. F. Verkuijlen, L. Lamagna, E. Langereis, S. Rushworth, F. Roozeboom, M. C. M. van de Sanden, and W. M. M. Kessels, J. Vac. Sci. Technol. A **29**, 021016 (2011).
[40]M. Popovici *et al.*, Chem. Mater. **29**, 4654 (2017).
[41]S.-J. Won, W.-D. Kim, C.-Y. Yoo, S.-T. Kim, Y.-W. Park, J.-T. Moon, and M.-Y. Lee, *International Electron Devices Meeting 2000. Technical Digest IEDM, San Francisco, CA, 10–13 December 2000* (IEEE, New York, 2000), pp. 789–792.
[42]M. L. Green, M. E. Gross, L. E. Papa, K. J. Schnoes, and D. Brasen, J. Electrochem. Soc. **132**, 2677 (1985).
[43]K. Fuchs, Math. Proc. Camb. Philos. Soc. **34**, 100 (1938).
[44]E. H. Sondheimer, Adv. Phys. **1**, 1 (1952).
[45]A. F. Mayadas and M. Shatzkes, Phys. Rev. B **1**, 1382 (1970).
[46]L. Pantisano *et al.*, Appl. Phys. Lett. **88**, 243514 (2006).
[47]V. Afanas'ev, N. Kolomiiets, M. Houssa, and A. Stesmans, Phys. Status Solidi A **215**, 1700865 (2017).
[48]E. H. Nicollian and J. R. Brews, *MOS (Metal Oxide Semiconductor) Physics and Technology* (Wiley, New York, 1982).
[49]R. Jha, J. Gurganos, Y. H. Kim, R. Choi, J. Lee, and V. Misra, IEEE Electron Device Lett. **25**, 420 (2004).
[50]Huang-Chun Wen *et al.*, IEEE Electron Device Lett. **27**, 598 (2006).
[51]K. Frohlich, K. Husekova, D. Machajdik, R. Luptak, M. Tapajna, and J. C. Hooker, *The Fifth International Conference on Advanced Semiconductor Devices and Microsystems, ASDAM 2004, Smolenice, Slovakia, 17–21 October 2004* (IEEE, New York, 2004), pp. 163–166.
[52]S. K. Dey, J. Goswami, D. Gu, H. de Waard, S. Marcus, and C. Werkhoven, Appl. Phys. Lett. **84**, 1606 (2004).
[53]S. Swaminathan, Y. Sun, P. Pianetta, and P. C. McIntyre, J. Appl. Phys. **110**, 094105 (2011).
[54]H. B. Michaelson, J. Appl. Phys. **48**, 4729 (1977).
[55]K. J. Park, J. M. Doub, T. Gougousi, and G. N. Parsons, Appl. Phys. Lett. **86**, 051903 (2005).
[56]Y.-S. Suh, H. Lazar, B. Chen, J.-H. Lee, and V. Misra, J. Electrochem. Soc. **152**, F138 (2005).
[57]S. Cwik, K. N. Woods, M. J. Saly, T. J. Knisley, and C. H. Winter, J. Vac. Sci. Technol. A **38**, 012402 (2019).
[58]See supplementary material at https://www.scitation.org/doi/suppl/10.1116/6.0001078 for NMR spectra.